

## Force and flow at the onset of drag in plowed granular media

Nick Gravish

*School of Physics, Georgia Institute of Technology, Atlanta, Georgia 30332, USA*

Paul B. Umbanhowar

*Department of Mechanical Engineering, Northwestern University, Evanston, Illinois 60208, USA*

Daniel I. Goldman

*School of Physics and School of Biology, Georgia Institute of Technology, Atlanta, Georgia 30332, USA*

(Received 29 December 2013; published 3 April 2014)

We study the transient drag force  $F_D$  on a localized intruder in a granular medium composed of spherical glass particles. A flat plate is translated horizontally from rest through the granular medium to observe how  $F_D$  varies as a function of the medium's initial volume fraction,  $\phi$ . The force response of the granular material differs above and below the granular critical state,  $\phi_c$ , the volume fraction which corresponds to the onset of grain dilatancy. For  $\phi < \phi_c$   $F_D$  increases monotonically with displacement and is independent of drag velocity for the range of velocities examined ( $< 10$  cm/s). For  $\phi > \phi_c$ ,  $F_D$  rapidly rises to a maximum and then decreases over further displacement. The maximum force for  $\phi > \phi_c$  increases with increasing drag velocity. In quasi-two-dimensional drag experiments, we use granular particle image velocimetry (PIV) to measure time resolved strain fields associated with the horizontal motion of a plate started from rest. PIV experiments show that the maxima in  $F_D$  for  $\phi > \phi_c$  are associated with maxima in the spatially averaged shear strain field. For  $\phi > \phi_c$  the shear strain occurs in a narrow region in front of the plate, a shear band. For  $\phi < \phi_c$  the shear strain is not localized, the shear band fluctuates in space and time, and the average shear increases monotonically with displacement. Laser speckle measurements made at the granular surface ahead of the plate reveal that for  $\phi < \phi_c$  particles are in motion far from the intruder and shearing region. For  $\phi > \phi_c$ , surface particles move only during the formation of the shear band, coincident with the maxima in  $F_D$ , after which the particles remain immobile until the sheared region reaches the measurement region.

DOI: [10.1103/PhysRevE.89.042202](https://doi.org/10.1103/PhysRevE.89.042202)

PACS number(s): 45.70.Cc, 83.80.Fg

Dry granular materials (GMs) are collections of macroscopic dissipative particles and are common in everyday life, from coffee grounds to sand. The constituents of a granular material are typically spherical particles (diameter  $\approx 100$   $\mu\text{m}$  or greater) that interact through short-range contact forces (friction and normal force). Physics studies of granular media have many engineering and biological applications [1–3] because granular matter is so prevalent in industry and nature.

Similar to fluids, GMs deform and flow under stress. Unlike Newtonian fluids, however, a GM requires a nonzero stress to induce flow, called the yield stress. A detailed understanding of the yielding process in granular materials is of fundamental importance to understanding how animals, tools, and robots interact with soil [1–3]. Plate drag is a particular example of a more general class of GM interactions called localized forcing that are relevant in the locomotion of organisms or robots [1–3]. Localized forcing of GM consists of a localized boundary that is displaced or rotated through an extended granular medium [4–14].

Understanding the force and flow response during localized forcing is complicated by the fact that the density, stress, and strain fields are spatially and temporally heterogeneous [15]. However many interactions with GM are localized and thus detailed understanding of the principles of localized forcing are needed. Recent studies of localized forcing, such as horizontal drag [15], vertical penetration [12,16–18], rotation of a plate within granular media [19], or impact experiments [20,21] have highlighted the important role the initial volume fraction  $\phi$  of the material plays in force and flow dynamics.

Granular material may compact (decrease in occupied volume) or dilate (expand in occupied volume) under an imposed shear depending on the initial  $\phi$  [22]. The sensitivity of drag to initial  $\phi$  is governed by this compaction-dilation flow response. A loosely packed GM (low  $\phi$ ) compacts under shear and thus strengthens, while a closely packed (high  $\phi$ ) media dilates (expands in volume) under shear in which the material weakens and forms persistent shear bands [15]. The  $\phi$  where the transition from compaction to dilation occurs is called the granular critical state  $\phi_c$  [22].

For quasistatically forced granular materials  $\phi$  typically varies between the random loose pack ( $\phi = 0.55$  [23]) and random close pack ( $\phi = 0.64$ ) limits for ideal monodisperse sphere packings. In practice however GM are typically found in a smaller range of volume fractions  $0.57 < \phi < 0.63$ . Granular materials with initial state  $\phi$  can be prepared through a combination of fluid flow and vibration [21,24]. In this study we investigate the role of  $\phi$  and in particular the distance to the critical state,  $\phi - \phi_c$  in determining force and flow dynamics during initial yielding of granular media.

In a previous paper we studied the spatial and temporal dynamics of granular drag resistance of a flat plate translated through dry granular material [15]. Here we study the transient drag force dynamics on a plate that is moved horizontally from rest to velocity  $v$  along the horizontal direction through granular media prepared at different  $\phi$ . Experiments are performed both in the bulk and adjacent to a transparent wall to visualize the subsurface granular flow below the surface.

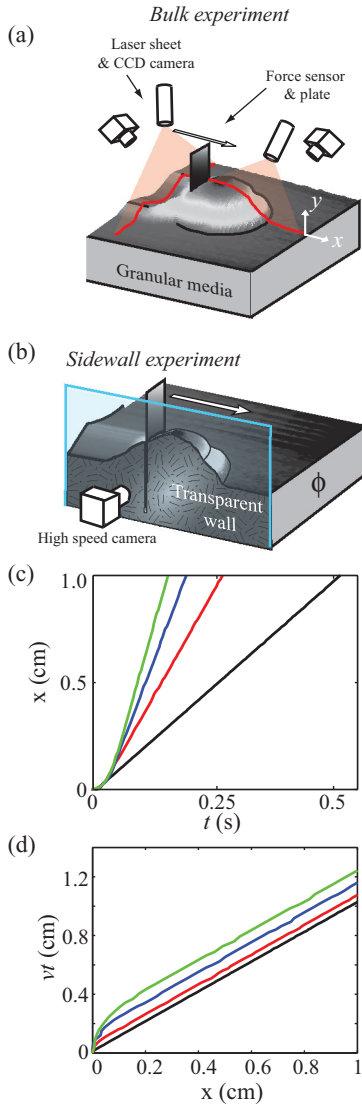


FIG. 1. (Color online) Drag measurements in granular media. (a) The bulk experiment consists of a partially submerged and vertical flat plate horizontally translated through granular media. Two laser lines and cameras measure surface deformation ahead of and behind the plate. (b) In the side-wall experiments the plate is placed against a transparent wall and high-speed video is recorded. (c) Displacement vs time for four speeds in glass beads (2 cm/s black, 4 cm/s red, 6 cm/s blue, 8 cm/s green). (d) Plate commanded velocity times time vs plate position. The desired velocity is reached within 100  $\mu\text{m}$  displacement for all speeds (2 cm/s black, 4 cm/s red, 6 cm/s blue, 8 cm/s green).

## I. METHODS

Drag measurements, see Fig. 1, were performed in a  $27 \times 86 \times 13 \text{ cm}^3$  bed of  $256 \pm 44 \text{ }\mu\text{m}$  glass beads (Potters Industries; density  $\rho = 2.51 \text{ g cm}^{-3}$ ). Similar responses to those described here were observed in other granular materials, including heterogeneous beach sand and poppy seeds. Air flow through the porous bed floor initially fluidized the medium, and then a combination of air flow (below fluidization) and mechanical vibration generated the desired initial volume fraction [ $0.579 < \phi < 0.619$ ; see Fig. 2(a)]. Air flow was

turned off prior to testing, and volume fraction was determined from bed height images as  $\phi = M/\rho Ah$ , where  $M$ ,  $A$ , and  $h$  are the bed mass, area, and height respectively.

A stepper motor and linear ball-screw translation stage displaced a 3.9 cm wide by 0.3 cm thick steel plate partially submerged to a variable fixed depth  $7.5 < d < 9.5 \text{ cm}$  over a total distance of 50 cm at constant speeds of  $v = 2, 4, 6, 8 \text{ cm s}^{-1}$ . An optical encoder on the stepper motor recorded the position of the linear translation stage carriage and a three-axis ATI load cell mounted between the submerged plate and translation stage measured the drag forces,  $F(t)$  (sampled at 200 Hz). The stiffness of the drag plate apparatus was  $k_{\text{plate}} = 145.7 \pm 0.1 \text{ N/cm}$ . We assume that during yielding the granular material and beam both act as elastic elements in series. From the known beam stiffness we calculate the displacement of the granular material as  $x_G = x(t) - F(t)/k_{\text{beam}}$ . In these experiments we only study the initial 1 cm of drag to observe the transient force and flow behavior at drag onset. However, steady-state drag observation was used to characterize the dilation response of the media at different initial  $\phi$  as described previously [15]. Using laser line profilometry, we recorded the resultant surface profile of the granular media and used it to quantify the change in vertical cross sectional area,  $\Delta A$ , normalizing by the submerged area of the plow,  $A_p = \text{width} \times \text{depth}$ . Profiles were measured 35 cm from the start of drag where the profile was in a steady state.

We also measured the time evolution of the granular surface along the direction of motion at the midplane of the plate. A laser line was used to illuminate the drag path and we placed a camera at an oblique side angle such that height changes in the granular surface corresponded to vertical motion of the laser line in the camera's image. We recorded video at 30 fps and tracked the surface height evolution in MATLAB.

In separate drag experiments used to characterize the flow, a flat plate at depth  $5.5 < d < 6.5 \text{ cm}$  was positioned against a transparent wall and displaced at  $v = 2 \text{ cm s}^{-1}$  parallel to the wall. The near-wall setup exhibited similar force fluctuations as the bulk but with approximately half the mean force, this method was described previously [15]. Video (250 fps) of the flow was recorded and analyzed in MATLAB using image registration with a correlation time of 0.02 s. The flow fields were evaluated on a grid spacing of  $2.0 \times 2.0 \text{ mm}$  and each time step between frames is 0.04 s. A pixel in the image corresponds to 203  $\mu\text{m}$  in distance and the PIV image registration algorithm returned a subpixel displacement to 1/10 a pixel dimension. We postprocessed our PIV velocity fields using a spatial median filter, commonly used in image processing, which reduced spurious velocity measures.

We removed systematic variations in the force—the decrease in depth of the constant height intruder with increasing  $\phi$ —by defining the drag force  $F_D$  as the raw drag force multiplied by a depth correction factor  $(\frac{d_{LP}}{d})^2$  normalized to the loose pack depth  $d_{LP}$ . Separate measurements at controlled intruder depth support this normalization technique.

In a final experiment we removed the lens from a CCD camera and pointed the sensor toward a laser spot (size  $\approx 3 \text{ mm}$ ) illuminating the surface 12 cm ahead of the plate's initial position. We imaged the reflected pattern of light from the laser, called a speckle pattern [25,26]. The speckle

pattern is the interference pattern from photon backscattering from the granular media and thus small changes in grain position near the laser spot appear as changes in the speckle field pattern. We validated speckle pattern measurements using two different experimental apparatus, and we also verified that the speckle pattern was shielded from motor vibration and stray reflected light.

## II. STATE PREPARATION AND CHARACTERIZATION

Air flow and vibration of varying durations were used to prepare granular media of initial volume fraction  $\phi$  [Fig. 2(a), error bars represent  $\pm 1$  SD from four repetitions] as in previous studies [15,21]. Initially the granular media was air fluidized to a bubbling state. Halting the air flow left the media in a loosely packed state (low  $\phi$ ). To compact the media, we used a combination of mechanical vibration and air flow below the onset of fluidization.

$\phi$  increased monotonically as a function of vibration duration [Fig. 2(a)]. The vibration mechanism, a motor with an off-axis mass, required a small time to start ( $t \approx 0.5$  s), and thus  $\phi$  did not vary for shake times less than this duration.

To characterize if the initial  $\phi$  was above the onset of dilatancy we used a previously described technique [15] in which we measured the cross-sectional area  $A$  of the trough left behind after drag with respect to the area of the plate  $A_p$ . Observing the difference in  $A$  after the drag we determined whether the material compacted ( $\frac{\Delta A}{A_p} < 0$ ), dilated ( $\frac{\Delta A}{A_p} > 0$ ), or remained the same ( $\frac{\Delta A}{A_p} = 0$ ).

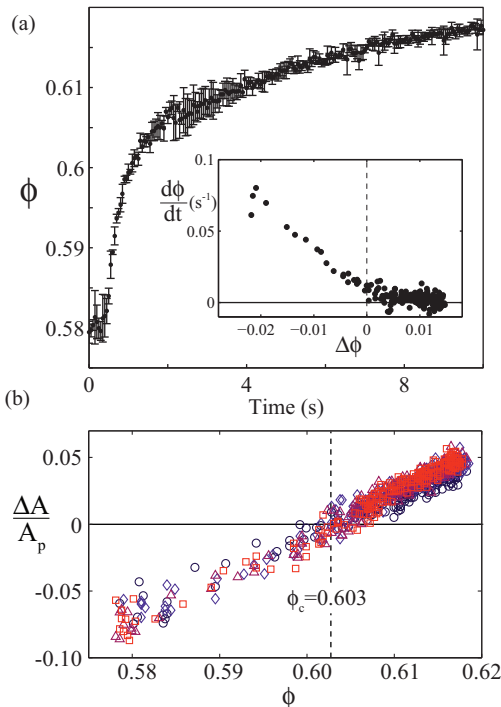


FIG. 2. (Color online) Compaction behavior of granular media. (a) Initial  $\phi$  vs vibration time. Error bars represent  $\pm 1$  SD of four replicates. Inset shows numerical derivative of  $\phi(t)$  vs  $\Delta\phi$ . (b) Compaction-dilation response of granular media vs initial  $\phi$  (2 cm/s circles, 4 cm/s diamonds, 6 cm/s triangles, 8 cm/s squares).

In these experiments the dilation transition occurred at  $\phi_c = 0.603 \pm 0.003$  as determined by the zero crossing of a best fit line [Fig. 2(b)]. We refer to the prepared granular state in terms of  $\Delta\phi = \phi - \phi_c$ , where  $\Delta\phi < 0$  is a loose-packed, compacting GM, and  $\Delta\phi > 0$  is a close-packed, dilating GM. Over the four different drag speeds tested,  $v = 2, 4, 6, 8$  cm  $s^{-1}$ , we observed no significant difference in measured  $\phi_c$  or in the compaction-dilation curves,  $\frac{\Delta A}{A_p}$ , which suggests that the average compaction-dilation response was independent of velocity for the speeds tested.

During packing of the granular material, the rate of increase in  $\phi$  differed as a function of the duration of mechanical vibration. We approximated the rate of compaction  $\frac{d\phi}{dt}$  with the numerical derivative, which is calculated as the mean slope of the  $\phi$  vs  $t$  curve over time bin widths of  $\pm 0.1$  s [inset Fig. 2(a)]. Examination of  $\frac{d\phi}{dt}$  illustrates that granular material rapidly compacts from an initially loose packing, and the rate of compaction decreases as the compaction increases. Although extensive research has been performed to investigate compaction dynamics of granular media [27–29] to our knowledge it is not known what, if any, role the dilation transition has on compaction dynamics.

## III. DRAG FORCE

The primary focus of this study is the force on an intruder dragged from rest within granular media of different initial  $\Delta\phi$ . The drag force  $F_D$  on a flat plate translated 1 cm horizontally was sensitive to initial  $\Delta\phi$  in both magnitude and functional form [Fig. 3(a)]. For  $\Delta\phi < 0$ ,  $F_D$  increased monotonically with  $x$  and thus was largest at the end of the 1 cm drag. However, for  $\Delta\phi > 0$ ,  $F_D$  rapidly rose to a maximum and subsequently decreased for the remainder of the 1 cm drag.

We determined the displacement of the plate at the granular surface by the displacement due to elastic loading of the plate. This allowed us to examine the yield force as a function of the displacement of granular material at the beam surface  $x_G$  [Fig. 3(b)]. We found that for the lowest values of  $\Delta\phi$  the grains began to move almost immediately in response to plate displacement. At low  $\Delta\phi$   $F_D$  slowly increased with  $x_G$  and was similar in shape to the force-displacement curve in the laboratory reference frame. As  $\Delta\phi$  increased the force exerted by the granular material at the onset of grain motion—defined as the yield force  $F_Y$ —increased with volume fraction [Figs. 3(b) and 4(a)].

The variation in drag force observed for increasing  $\Delta\phi$  is similar to that observed for underconsolidated and overconsolidated soils under deformation [22]. In the critical state soil mechanics model [22] it is assumed that soil, under constant boundary-driven shear, will either dilate or compact depending on initial  $\phi$  and the instantaneous density  $\phi(t)$  will approach a critical  $\phi_c$ . When the system evolves to this critical state no further force change is observed. For comparison we note that the drag force in media prepared near  $\Delta\phi = 0$  [highlighted in bold in Fig. 3(a)] is flat (unchanging with displacement) after 2 mm of drag and partitions the  $F_D$  curves between compacting GM (below) and dilating GM (above) with all curves approaching a similar value at 1 cm.

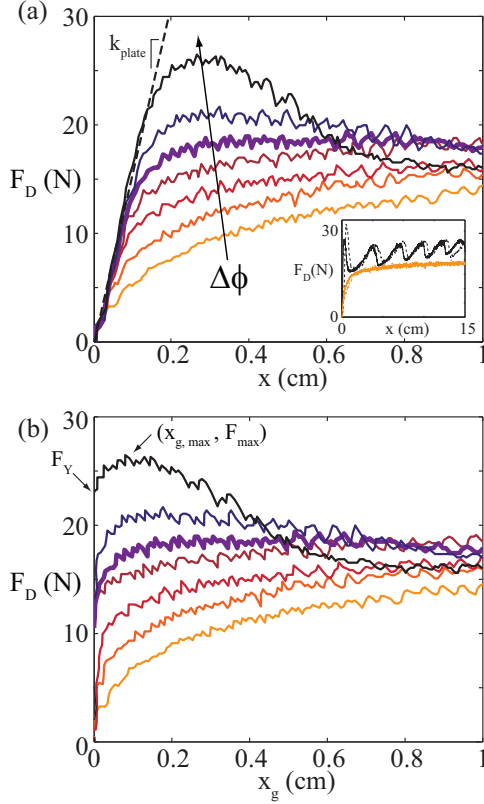


FIG. 3. (Color online) (a) Force vs displacement at different initial  $\Delta\phi$  for  $v = 2$  cm/s. Arrow indicates curves of increasing initial  $\Delta\phi$  (in increments of  $\approx 0.006$ ). Bold curve is near critical packing at  $\Delta\phi = 0.001$ . Inset shows temporal evolution of  $F_D$  over greater displacements. Curves with  $\Delta\phi > 0$  (black) and  $\Delta\phi < 0$  (orange) at  $v = 2$  cm/s (solid line) and  $v = 8$  cm/s (dashed line) are shown. (b) Force vs grain displacement at different initial  $\Delta\phi$ . Arrow on y axis shows the yield force,  $F_Y$ .

We quantify the variation in  $F_D$  as a function of  $\Delta\phi$  by computing several metrics of the drag force [Figs. 4(a)–4(d)]. The yield force,  $F_Y$  increased monotonically with  $\Delta\phi$  for all volume fractions [Fig. 4(a)]. There was a slight speed dependence on  $F_Y$  in which drags with  $v = 8$  cm/s had slightly larger yield forces than the slower drags. By linearly extrapolating the  $\Delta\phi < 0$  yield force to  $F_Y = 0$ , we find that  $\phi$  at the onset of nonzero yield force is  $\phi = 0.569 \pm 0.005$ . This volume fraction is near the random-loose pack volume fraction, which in turn is the lower limit for random, mechanically stable granular materials [23].

The maximum drag force  $F_{\max}$  increased linearly with  $\Delta\phi$  in both low and high  $\Delta\phi$  regimes, however the slope of this curve exhibited a discontinuity near  $\Delta\phi = 0$  [Fig. 4(b)]. The change in slope reflects the onset of the maxima in  $F_D$  above  $\phi_c$  [see Fig. 3(a)]. Similar changes in granular resistance force across a critical  $\phi$  have been previously observed in penetration [18] and shear [17].

To determine at which  $\Delta\phi$  the onset of a force maximum occurs we compare the maximum of  $F_D$  over the 1 cm drag with  $F_D$  at  $x = 1$  cm [Fig. 4(c)]. If this ratio,  $\tilde{F}_{\max} = \frac{F_{\max}}{F_D(x=1\text{ cm})}$ , is unity the drag force is monotonically increasing and if the ratio exceeds unity a maximum exists. Figure 4(b) indicates

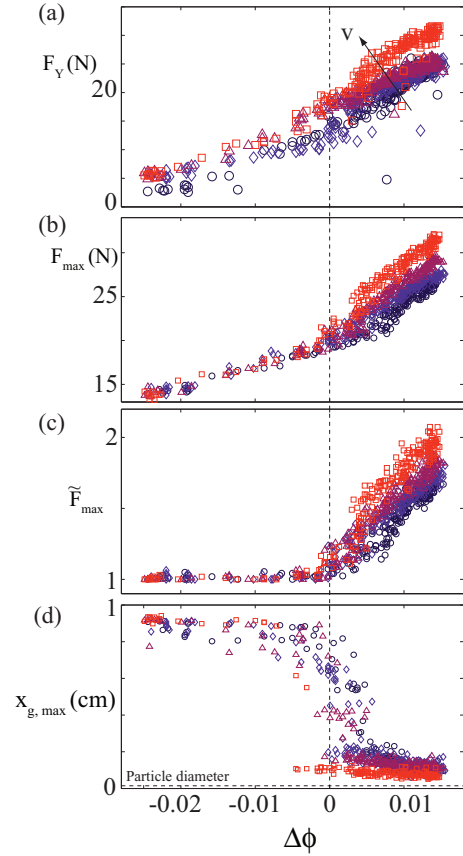


FIG. 4. (Color online) Yield force metrics vs initial  $\Delta\phi$  for four separate drag speeds (2 cm/s circles, 4 cm/s diamonds, 6 cm/s triangles, 8 cm/s squares). (a) Yield force of granular medium. Arrow indicates trend of increasing drag speed. (b) Peak force developed over 1 cm displacement. (c) Peak force developed over 1 cm displacement normalized by force at  $x = 1$  cm. (d) Plate displacement at peak force.

that the onset of a maximum in  $F_D$  occurs at  $\Delta\phi = 0$  independent of drag speed.

We define the grain displacement  $x_g$  at  $F_{\max}$  as  $x_{g,\max}$ . For  $\Delta\phi < 0$ ,  $x_{g,\max}$  occurred near the end of the 1 cm drag because  $F_D$  increases monotonically. For  $\Delta\phi > 0$  however  $x_{g,\max}$  occurred at a shorter distance and was roughly independent of speed. For the highest volume fraction regime ( $\Delta\phi > 0.1$ )  $x_{g,\max} = 0.10 \pm 0.03$  cm, which corresponds to approximately 40 particle diameters [horizontal dashed line in Fig. 4(d) shows particle diameter]. We expect that  $x_{g,\max}$  will scale with particle diameter and intruder geometry although the details of this scaling are unknown.

As shown in Figs. 3 and 4 the drag force exhibits several signatures of a bifurcation across the dilation transition,  $\Delta\phi = 0$ . The development of a local maximum in  $F_D$  as  $\Delta\phi$  exceeds zero indicates a change in failure dynamics similar to a ductile to brittle transition that occurs in solids [30]. Although the shape of  $F_D$  varied sharply across  $\Delta\phi = 0$ , the yield force increased over the range of  $\Delta\phi$  and exhibited only a slight change in slope across  $\Delta\phi = 0$ . We suspect that a bifurcation in  $F_Y$  across  $\Delta\phi = 0$  does not occur because the effect of dilatancy, which is the cause of the force and flow

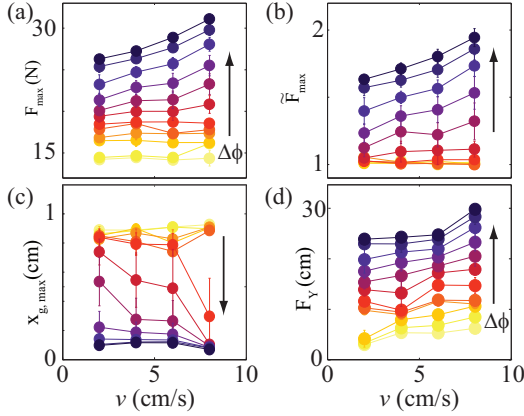


FIG. 5. (Color online) Speed dependence of drag force for different initial  $\Delta\phi$ . Colors represent initial  $\Delta\phi$  and arrows indicate direction of increasing  $\Delta\phi$  in increments of 0.003. (a)  $F_{\max}$  vs speed. (b)  $\tilde{F}_{\max}$  vs speed. (c)  $x_{g,\max}$  vs speed. (d)  $F_Y$  vs speed.

bifurcation at  $\Delta\phi = 0$  [15], is only relevant after grain motion is initiated.  $F_Y$  is a measurement of the force developed before grain motion and thus it is likely that dilation-compaction dynamics do not influence this force. Instead we observed that  $F_Y$  increased approximately linearly with  $\Delta\phi$ . We also observed that  $F_Y$  vanished as  $\phi$  approached the random-loose pack limit of granular material. These observations are in accord with recent experimental results using vane [19] and penetration geometries [17], and the linear increase in yield force is likely a result of the linear increase in contact number in the packing [31].

Surprisingly we observed a speed dependence of  $F_D$ , which has not been seen at low velocities in steady-state drag experiments. Previous studies of steady-state granular drag forces have found that in the slow drag regime ( $v < 10$  cm/s) drag force is insensitive to  $v$  [6,17,32]. To quantify the functional dependence of drag force on  $v$  we averaged  $F_{\max}$ ,  $\tilde{F}_{\max}$ ,  $x_{g,\max}$ , and  $F_Y$  over bins of  $[\phi, \phi + 0.003]$  and plotted the results as a function of drag speed [Figs. 5(a)–5(d)]. The quantities associated with the drag force magnitude and shape,  $F_{\max}$  and  $\tilde{F}_{\max}$ , exhibited no speed dependence at low  $\Delta\phi$  and increased with  $v$  at high  $\Delta\phi$  [Figs. 5(a) and 5(b)].  $x_{g,\max}$  however displayed more complex speed dependence [Fig. 5(c)]. Increasing drag speed did not influence the value of  $x_{g,\max}$  in the high and low  $\Delta\phi$  regimes however, for intermediate packings near  $\Delta\phi = 0$ ,  $x_{g,\max}$  decreased with increasing speed [Fig. 5(c)].  $F_Y$  varied only slightly with  $v$  at low  $\Delta\phi$  and it was unclear whether  $F_Y$  was sensitive to  $v$  at higher packing fractions [Fig. 5(d)].

To determine the onset of speed dependence in  $F_D$  we measured the slope of linear fits to the force-speed curves ( $\frac{\Delta F_{\max}}{\Delta v}$  and  $\frac{\Delta \tilde{F}_{\max}}{\Delta v}$ ) in Figs. 5(a) and 5(b). As a function of  $\Delta\phi$  we observed that the onset of nonzero  $\frac{\Delta F_{\max}}{\Delta v}$  and  $\frac{\Delta \tilde{F}_{\max}}{\Delta v}$  occurred near  $\Delta\phi = 0$  [Figs. 6(a) and 6(b)]. This indicates that the drag force depends on speed only when the media is dilatant.

Our experiment is consistent with a lack of  $v$  dependence in the steady-state (inset Fig. 3 and [15]). However, the speed-dependent behavior we observe during drag onset is not understood. The speed dependence of the yield force is likely

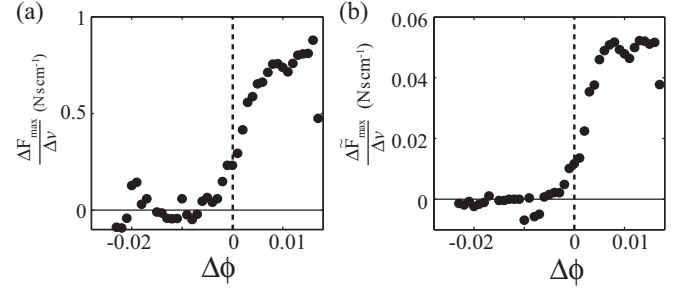


FIG. 6. Speed dependence of drag force vs initial  $\Delta\phi$ . Slope of linear fit to (a)  $F_{\max}(v)$  and (b)  $\tilde{F}_{\max}(v)$  in Fig. 5.

due to the acceleration of the body of granular material—the added mass—in front of the plate from rest to speed  $v$ . Such an added mass effect is readily observed for accelerating bodies within fluids [33], however the origin of the  $\Delta\phi$ -dependent added mass in granular materials remains unknown.

#### IV. SURFACE FLOW

We now study the flow behavior of the granular material during yielding to better understand the mechanism responsible for the dependence of  $F_D$  on  $\Delta\phi$ . The displaced granular material in front of the translated plate forms a hill, which can be seen when viewed from an oblique side angle (Fig. 7). We illuminate the granular surface during yield with a laser line and record video from a low-angle side view (see inset Fig. 7).

After yield the hill height in front of the plow depended upon initial  $\Delta\phi$  [Fig. 8(a)]. In general we observed that the hill height increased for increasing  $\Delta\phi$ . We computed two measures of the hill shape, the maximum hill height  $y_{\max}$ , and the total cross sectional area of the hill  $A_{\text{hill}}$ , and these are plotted in Figs. 8(b) and 8(c).

The increase in hill cross-sectional area with increasing  $\Delta\phi$  is a result of the transition from compaction to dilation. As shown in Fig. 2(b) the volume change that occurs in the granular material in steady-state drag increases linearly with  $\Delta\phi$ . Thus the hill height and cross-sectional area—measures of the volume change from the mobile grains—should linearly increase with  $\Delta\phi$ .

Although we observed that hill shape was influenced by  $\Delta\phi$  we did not observe a signature of  $\phi_c$ . Thus to identify features of the bifurcation in grain dynamics that occurs at  $\Delta\phi = 0$  we must look to other methods to characterize the flow response.

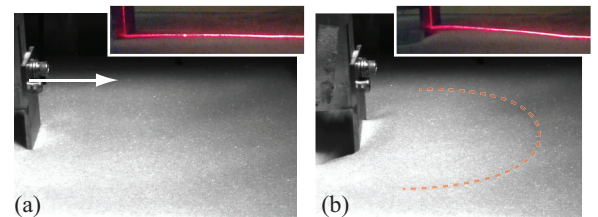


FIG. 7. (Color online) Oblique side view of surface deformation during yield. (a) Initial position of plate. Arrow indicates direction of motion. (b) Final position of plate after 1 cm drag. Insets show surface profiles using laser line.

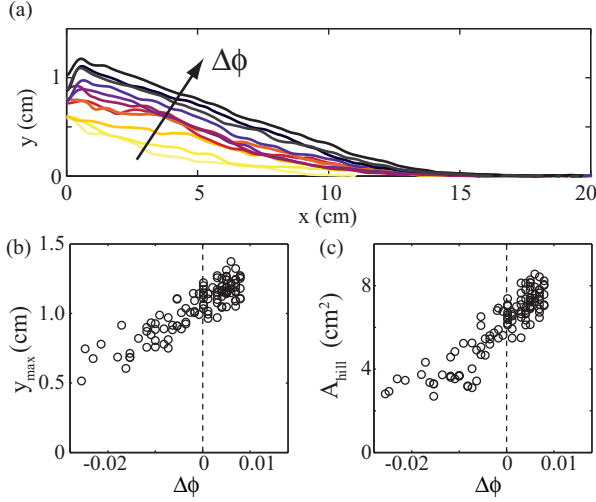


FIG. 8. (Color online) Surface deformation characteristics during drag. (a) Surface profile after 1 cm drag measured with a laser line technique. Arrow indicates trend for increasing initial  $\Delta\phi$ . (b) Maximum hill height vs initial  $\Delta\phi$ . (c) Cross sectional area of hill vs initial  $\Delta\phi$ .

## V. BULK FLOW

Similar to our previous study we performed plate drag experiments at  $v = 2 \text{ cm s}^{-1}$  next to a transparent wall [15]. This allowed visualization of the granular flow in the bulk during yielding. From particle image velocimetry we determined the velocity field,  $\vec{u}$ , of the flowing granular media (Fig. 9). In general, independent of  $\Delta\phi$ , we observed the flow to occur in a wedge-shaped region directly in front of the plate (Fig. 9) consistent with our previous study [15]. The granular media was pushed by the plate in the positive  $x$  direction and subsequently flowed towards the surface in the positive  $y$  direction as if up an inclined plane. This flow pattern is consistent with a Coulomb wedge-type failure mode of granular media and observations of similar flow patterns have been previously reported [9,10,34]. During plate drag experiments against the transparent wall,  $F_D$  is composed of a granular resistance force and a frictional force from the plate-wall interface. Thus in side-view experiments we restrict our analysis of force displacement to the actuator displacement,  $x$ .

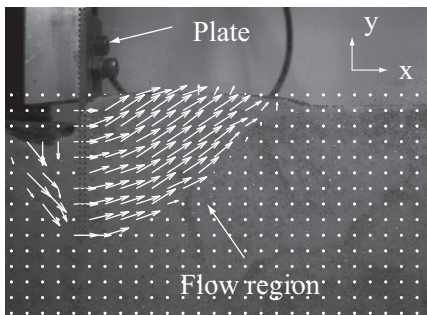


FIG. 9. Side view of flow visualization experiment at  $\Delta\phi = 0.01$ . Velocity field from particle image velocimetry superimposed. Vector tails are separated by 0.93 cm.

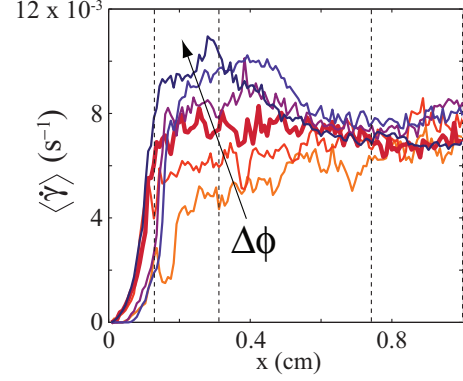


FIG. 10. (Color online) Spatial average of the maximal shear strain rate vs displacement. The four dashed lines indicate the four displacements at which the shear strain rate field is plotted in Fig. 12.

Friction force associated with shear strain plays an important role in quasistatic granular dynamics. Thus to understand the changes in  $F_D$  at different initial  $\Delta\phi$  we study the shear strain of the flow field. To determine the maximum shear strain rate of the granular flow we compute the components of the two-dimensional deformation rate tensor: the normal strain rate,  $\dot{e}_{ii} = \frac{du_i}{dt}$  ( $i = x, y$ ), and the average shear strain rate,  $\dot{e}_{xy} = \frac{1}{2}(\frac{du_x}{dy} + \frac{du_y}{dx})$ . The maximum shear that occurs in the flowing region is then found by solving for the maximal shear strain rate field  $\dot{\gamma} = \sqrt{(\frac{\dot{e}_{xx} - \dot{e}_{yy}}{2})^2 + \dot{e}_{xy}^2}$  and its spatial average  $\langle \dot{\gamma} \rangle$  over the observation area [16].

The time evolution of  $\langle \dot{\gamma} \rangle$  during drag was sensitive to initial  $\Delta\phi$  and was remarkably similar to  $F_D$  in shape (Fig. 10). For  $\Delta\phi < 0$ ,  $\langle \dot{\gamma} \rangle$  increased monotonically (neglecting rapid fluctuations) over the drag while for  $\Delta\phi > 0$ ,  $\langle \dot{\gamma} \rangle$  exhibited a maximum consistent with the maximum in  $F_D$  that occurs in  $\Delta\phi > 0$  (Fig. 3). Similar to  $F_D$ ,  $\phi_c$  partitions  $\langle \dot{\gamma} \rangle$  to  $\Delta\phi < 0$  (below) and  $\Delta\phi > 0$  (above) packed responses. The similarity in  $F_D$  and  $\langle \dot{\gamma} \rangle$  over the course of the drag shows that, despite the complex flows that occur in the granular medium, a linear stress-strain relationship describes the granular rheology even for large displacements.

To compare the shear strain rate statistics with those of  $F_D$ , we compute the normalized maximum shear strain rate,  $\langle \tilde{\gamma} \rangle = \frac{\max\{\dot{\gamma}\}}{\dot{\gamma}(x=1 \text{ cm})}$  and the drag distance at which this local maximum occurs. Comparison of  $\langle \tilde{\gamma} \rangle$  and  $\tilde{F}_{\max}$  shows that they are also similar in form [Fig. 11(a)]. Furthermore the displacement at which the local maxima in both  $\langle \tilde{\gamma} \rangle$  and  $\tilde{F}_{\max}$  occurs is also similar indicating that when drag force is maximum the shear strain is also maximum [Fig. 11(b)]. The signature of the bifurcation at  $\Delta\phi = 0$  is clearly seen in both the flow and force measurements of Fig. 11.

To identify the mechanisms responsible for the variation of  $\langle \tilde{\gamma} \rangle$  with  $\Delta\phi$  we visualized the shear strain rate field,  $\dot{\gamma}$ , at four instances of time during displacement for three distinct initial  $\Delta\phi$  (Fig. 12). For all experiments, independent of  $\Delta\phi$ , we observed that shear strain was concentrated in a region—a shear band—which originated at the bottom of the plate and extended upwards to the surface.

Although shear bands were observed in the velocity fields at all  $\Delta\phi$ , the spatiotemporal dynamics and stability of these

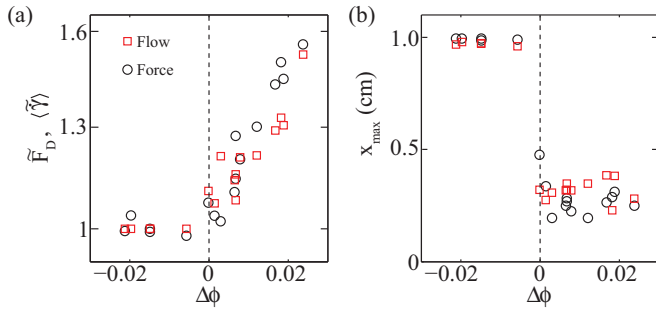


FIG. 11. (Color online) Comparison of yield force and shear strain statistics at different  $\Delta\phi$ . (a) Normalized peak drag force ( $\bar{F}_D$ , black circles) and average shear strain rate ( $\langle \dot{\gamma} \rangle$ , red squares) vs  $\Delta\phi$ . (b) Drag distance at maximum  $F_D$  (black circles) and maximum  $\langle \dot{\gamma} \rangle$  (red squares).

shear bands differed as a function of  $\Delta\phi$  (Fig. 12). Only for  $\Delta\phi > 0$  did we observe that shear bands remained localized in space. At  $\Delta\phi < 0$  the shape of the shear band emanating from the bottom of the plate fluctuated throughout the duration of the drag.

In Fig. 13 we display the spatiotemporal evolution of the shear band by plotting  $\dot{\gamma}$  evaluated along a horizontal strip in front of the plate [dashed line in middle right box, Fig. 12] vs time. Space-time plots of  $\dot{\gamma}$  in Fig. 13 illustrate the unsteady nature of the shear band for  $\Delta\phi < 0$ , and the onset of spatially localized shear (white arrows) for  $\Delta\phi > 0$ . For quantitative comparison of the magnitude of  $\dot{\gamma}$  in the flowing region, we plot shear strain rate profiles in front of the plate [Fig. 13(b)] evaluated after 0.8 cm of drag [white dashed line in Fig. 13(a)]. Similar evolution of the shear strain rate during shear band formation of a dilating GM has been observed in discrete element method simulations of a triaxial test [35].

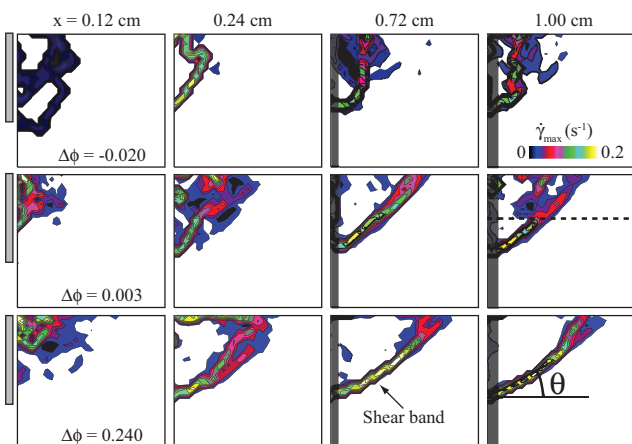


FIG. 12. (Color online) Maximal shear strain rate fields in fixed world reference frame for three  $\Delta\phi$  preparations (rows) at four displacements (columns). Box dimensions are  $9.74 \times 9.74$  cm. The gray bar on the left side of  $x = 0.12$  cm fields shows the initial plate location, which is advancing to the right. Gray regions in last two columns show region over which plate displaced. A stable shear band is highlighted for  $\Delta\phi = 0.240$  at  $x = 0.72$  cm. The shear band is oriented at an average angle  $\theta$  from the horizontal.

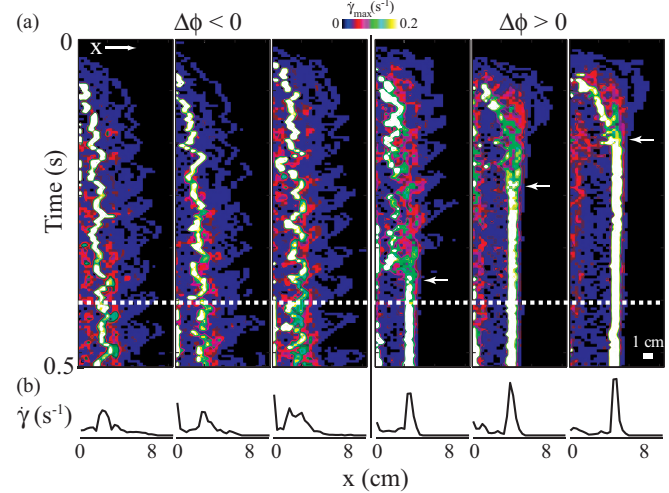


FIG. 13. (Color online) Spatiotemporal evolution of  $\dot{\gamma}$ . (a) Space-time plot of  $\dot{\gamma}$  at six initial  $\Delta\phi$  ( $-0.020, -0.015, -0.014, 0.003, 0.007, 0.024$ ; increasing from left to right).  $\dot{\gamma}$  is evaluated at a depth of 4 cm (see dashed line in middle right plot in Fig. 12). Width of space-time plot is 9.74 cm. White arrows in right three plots show onset of shear band stability. (b) Profile of  $\dot{\gamma}$  after  $x = 0.8$  cm drag distance. All curves are at same scale.

To characterize the shear band dynamics we measured the angle of the shear band near the bottom of the plate,  $\theta$ , and the plate displacement required before the onset of shear band stability (white arrows in Fig. 13). We did not observe the formation of stable shear bands for  $\Delta\phi < 0$  [open symbols, Fig. 14(a)]. For  $\Delta\phi > 0$  we observed that the drag distance before the onset of shear band stability decreased with increasing  $\Delta\phi$ . This is likely due to the dilation process that weakens the sheared region and allows for the formation of the stable shear band. We hypothesize that a dilation threshold must be reached before a shear band is formed. This would explain why as  $\Delta\phi$  increases, dilation and shear band formation occur more rapidly.

The shear band angle  $\theta$  (measured with respect to the horizontal) averaged over the last 0.36 cm of drag decreased approximately linearly with increasing  $\Delta\phi$  with best fit line  $\theta = (-368.3^\circ)\Delta\phi + 38.1^\circ$  [Fig. 14(b)]. Furthermore, as can be seen by the scatter in  $\theta$ , the temporal fluctuations in  $\theta$  decreased by more than twofold across  $\phi_c$ , see the inset in Fig. 14(b). This is another indication of the onset of shear band stability across the dilation transition.

The minimum shear plane angle for plate drag may be related to the internal friction angle of a granular material through the equation

$$\theta_{\min} = \tan^{-1}(\sqrt{\mu^2 + 1} - \mu) \quad (1)$$

(see Ref. [15] for derivation). We assume that during yielding the minimum material fails along the minimum shear plane angle [15] and thus we numerically solve for  $\mu$  from the linear relationship between  $\theta$  and  $\Delta\phi$ . We restrict our solutions to the range  $\mu \in [0, 1]$ . We plot  $\mu(\Delta\phi)$  in Fig. 14(c) and find that internal friction is 0 below  $\Delta\phi \approx -0.2$  and increases with  $\Delta\phi$  above  $\Delta\phi \approx -0.2$ . The observation of  $\mu = 0$  below  $\Delta\phi \approx -0.2$  may explain why we are unable to achieve volume

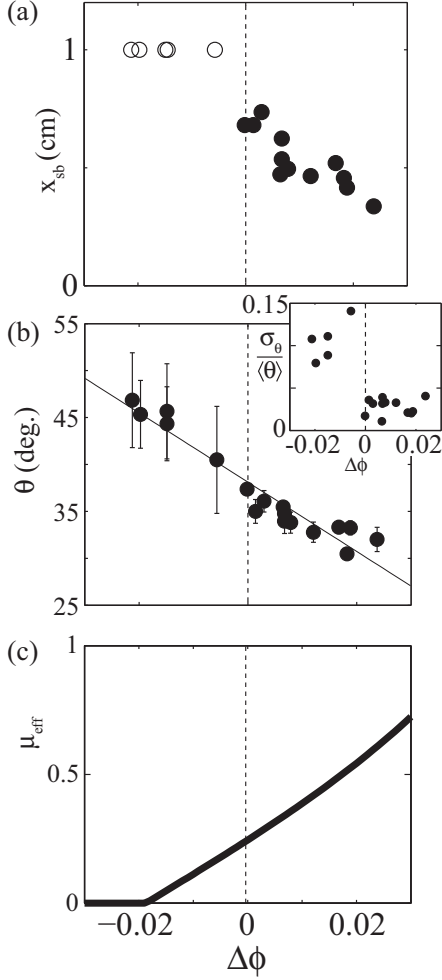


FIG. 14. Metrics of shear band formation and stability. (a) Drag distance at onset of stable shear band. Open circles indicate unstable shear band at end of 1 cm displacement. (b) Average angle of shear band,  $\theta$ , over last 0.36 cm of drag vs  $\Delta\phi$ . Line is best fit described in text. Error bars are  $\pm\sigma_\theta$ . Inset shows normalized fluctuation in  $\theta$  over last 0.36 cm of drag vs  $\Delta\phi$ . (c) Predicted internal friction angle from Eq. (1).

fractions below  $\Delta\phi \approx -0.2$  in experiment since below this the pile would be unstable.

The onset of granular flow for  $\Delta\phi > 0$  induces a large region of shear in the bulk, which, because of the dilatant nature of the  $\Delta\phi > 0$  material, results in rapid failure along a shear band. For  $\Delta\phi < 0$  however  $F_D$  slowly increases as the material strengthens under the induced shear. This transition from hardening to weakening is well understood in the context of critical state soil mechanics [22].

## VI. LASER SPECKLE MEASUREMENTS OF FAST FLUCTUATIONS

Finally we examine the unjamming response of the granular media ahead of the plate as a function of initial  $\phi$ . We observed microscopic grain motion at a point 12 cm ahead of the initial plate position. This position was chosen because it lies outside of the shear band zone that forms for  $\Delta\phi > 0$ , and thus we

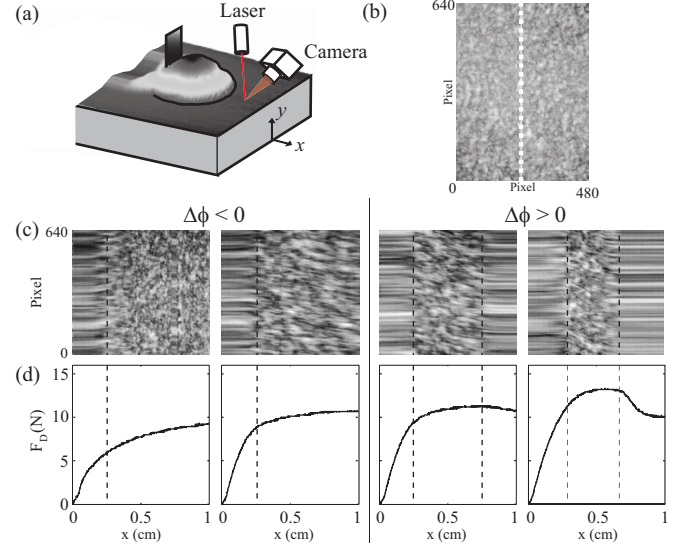


FIG. 15. (Color online) Laser speckle measurement of granular flow near the surface. (a) A laser illuminates the granular surface 12 cm ahead of the plate's initial position. (b) Sample image from the camera. We study the temporal evolution of the speckle pattern along the dashed line. (c) Space-time evolution of the speckle pattern at four different initial  $\Delta\phi$  (increasing from left to right). Dashed lines show jamming and unjamming of granular media during drag as evidenced by the transition between stationary and rapidly fluctuating regions in the space-time image  $x$ -axis is same as in (d). (d)  $F_D$  versus displacement during speckle measurement.

may study the motion of granular material outside of this region. We monitored grain motion by imaging the interference pattern of backscattered laser light on a CCD sensor; this pattern is called a laser speckle pattern [25,26] [Figs. 15(a) and 15(b)]. The speckle pattern is sensitive to minute changes in grain position—subnanometer displacements—and is thus a sensitive measure of grain motion near the surface.

To observe temporal dynamics we construct a space-time image of the speckle pattern by evaluating the speckle along a single row of pixels [white line in Fig. 15(b)]. The speckle dynamics show an initial period where the material is jammed [horizontal streaks in Fig. 15(c)] followed by an unjamming event in which the surface grains are set in motion. The force and speckle pattern dynamics are consistent with our previous observations. For  $\Delta\phi < 0$   $F_D$  slowly increases and the GM is constantly in motion while for  $\Delta\phi > 0$  a maximum in  $F_D$  is observed and this corresponds with a rejamming of the material [Figs. 15(c)–15(d)].

The rapid fluctuations in the speckle pattern that occur at  $\Delta\phi < 0$  indicate the granular material is constantly in a state of rearrangement. The speckle field indicates that small-scale motion of the grains occurs in loose-packed media even at distances far ahead of the plate where no noticeable surface motion can be viewed by eye [36]. In  $\Delta\phi > 0$  material however, the jamming event associated with the force drop in  $F_D$  is a result of the formation of a stable shear band. When stable shear bands form (like those shown in Fig. 12) the laser spot is far enough ahead of the plate such that it is outside this flowing region. Thus the laser speckle measurement indicates

that once the shear band forms (see  $\delta\phi > 0$  panels in Fig. 15) flow outside of the wedge region ceases and the flow is isolated to within the plate-shear band region.

## VII. CONCLUSION

We have investigated the force and flow response during onset of motion in granular material by a localized intruder as a function of initial volume fraction  $\phi$ . As in a previous experiment [15] we identified the volume fraction corresponding to the onset of dilation under shear,  $\phi_c$ , and showed that the dynamics of force and flow qualitatively differ across this transition. Similar observations of varying failure modes as a function of initial  $\phi$  have been made in avalanche [37,38] experiments, and indicate that granular failure is sensitive to volume fraction across a range of perturbation methods. Our experiments highlight a number of nontrivial phenomena associated with granular drag and its dependence on  $\Delta\phi$ . Our results illustrate that the role of the initial volume fraction of the granular media cannot be ignored when the forces and flows of granular materials are considered.

Speed independence of steady-state drag force in granular materials has been previously observed for slowly sheared systems [6,17,32]. However during drag onset we observed a speed dependence on  $F_D$  for  $\Delta\phi > 0$ . We hypothesize that the speed dependence during onset of motion is due to an added mass effect in which the granular medium is accelerated from

rest, however the  $\Delta\phi$  dependence of this phenomenon is not well understood.

From critical state soil mechanics it is known that the value of  $\phi_c$  depends upon the properties of the individual grains (friction, shape, etc.) and upon the confining pressure of the ensemble [22,35]. We are led to consider how, if at all, the dilation transition is related to the jamming transition of granular materials. This has been the subject of recent experimental [39] and theoretical [40] studies. However the connection between the critical state volume fraction and the jamming transition is unknown.

In this study we have shown that from a simple experiment—plate drag through granular material—we can observe sensitive dependence of the drag force on the initial conditions and experimental parameters. Such experiments will prove useful to further elucidate the failure modes of granular material as a function of prepared  $\phi$ . The complex interactions of animals, tools, and robots with soil [1–3] highlight the need to better understand how granular material behaves under stress during such intrusion events. Plate drag is a canonical example of localized forcing and is especially relevant for the development of robotic devices [3,41] and understanding biological locomotion [1,2].

## ACKNOWLEDGMENT

Funding provided by the Burroughs Wellcome Fund, ARL MAST CTA, ARO Grant No. W911NF-11-1-0514, and NSF Physics of Living Systems.

- 
- [1] R. Maladen, Y. Ding, C. Li, and D. Goldman, *Science* **325**, 314 (2009).
  - [2] N. Mazouchova, N. Gravish, A. Savu, and D. Goldman, *Biol. Lett.* **6**, 398 (2010).
  - [3] C. Li, P. Umbanhowar, H. Komsuoglu, D. Koditschek, and D. Goldman, *Proc. Natl. Acad. Sci. USA* **106**, 3029 (2009).
  - [4] R. Candelier and O. Dauchot, *Phys. Rev. Lett.* **103**, 128001 (2009).
  - [5] J. Geng, D. Howell, E. Longhi, R. P. Behringer, G. Reydellet, L. Vanel, E. Clément, and S. Luding, *Phys. Rev. Lett.* **87**, 035506 (2001).
  - [6] R. Albert, M. A. Pfeifer, A. L. Barabási, and P. Schiffer, *Phys. Rev. Lett.* **82**, 205 (1999).
  - [7] I. Albert, P. Tegzes, B. Kahng, R. Albert, J. G. Sample, M. Pfeifer, A. L. Barabási, T. Vicsek, and P. Schiffer, *Phys. Rev. Lett.* **84**, 5122 (2000).
  - [8] G. Hill, S. Yeung, and S. Koehler, *Europhys. Lett.* **72**, 137 (2005).
  - [9] Y. Ding, N. Gravish, and D. I. Goldman, *Phys. Rev. Lett.* **106**, 028001 (2011).
  - [10] A. Seguin, Y. Bertho, P. Gondret, and J. Crassous, *Phys. Rev. Lett.* **107**, 048001 (2011).
  - [11] F. Q. Potiguar, *Phys. Rev. E* **84**, 061302 (2011).
  - [12] E. Hamm, F. Tapia, and F. Melo, *Phys. Rev. E* **84**, 041304 (2011).
  - [13] E. Kolb, J. Cviklinski, J. Lanuza, P. Claudin, and E. Clément, *Phys. Rev. E* **69**, 031306 (2004).
  - [14] D. J. Costantino, J. Bartell, K. Scheidler, and P. Schiffer, *Phys. Rev. E* **83**, 011305 (2011).
  - [15] N. Gravish, P. B. Umbanhowar, and D. I. Goldman, *Phys. Rev. Lett.* **105**, 128301 (2010).
  - [16] T. G. Murthy, E. Gnanamanickam, and S. Chandrasekar, *Phys. Rev. E* **85**, 061306 (2012).
  - [17] J. Métayer, D. Suntrup III, C. Radin, H. Swinney, and M. Schröter, *Europhys. Lett.* **93**, 64003 (2011).
  - [18] M. Schröter, S. Nägle, C. Radin, and H. Swinney, *Europhys. Lett.* **78**, 44004 (2007).
  - [19] V. B. Nguyen, T. Darnige, A. Bruand, and E. Clement, *Phys. Rev. Lett.* **107**, 138303 (2011).
  - [20] P. Umbanhowar and D. Goldman, *Am. J. Phys.* **74**, 720 (2006).
  - [21] P. Umbanhowar and D. I. Goldman, *Phys. Rev. E* **82**, 010301 (2010).
  - [22] A. Schofield and P. Wroth, *Critical State Soil Mechanics* (McGraw-Hill, London, 1968).
  - [23] M. Jerkins, M. Schröter, H. L. Swinney, T. J. Senden, M. Saadatfar, and T. Aste, *Phys. Rev. Lett.* **101**, 018301 (2008).
  - [24] R. Ojha, N. Menon, and D. J. Durian, *Phys. Rev. E* **62**, 4442 (2000).
  - [25] D. I. Goldman and H. L. Swinney, *Phys. Rev. Lett.* **96**, 145702 (2006).
  - [26] D. Pine, D. Weitz, P. Chaikin, and E. Herbolzheimer, *Phys. Rev. Lett.* **60**, 1134 (1988).
  - [27] P. Richard, M. Nicodemi, R. Delannay, P. Ribière, and D. Bideau, *Nat. Mater.* **4**, 121 (2005).
  - [28] J. B. Knight, C. G. Fandrich, C. N. Lau, H. M. Jaeger, and S. R. Nagel, *Phys. Rev. E* **51**, 3957 (1995).
  - [29] P. Philippe and D. Bideau, *Europhys. Lett.* **60**, 677 (2002).

- [30] Y. Ben-Zion, K. A. Dahmen, and J. T. Uhl, *Pure Appl. Geophys.* **168**, 2221 (2011).
- [31] T. S. Majmudar, M. Sperl, S. Luding, and R. P. Behringer, *Phys. Rev. Lett.* **98**, 058001 (2007).
- [32] D. Chehata, R. Zenit, and C. Wassgren, *Phys. Fluids* **15**, 1622 (2003).
- [33] G. Falkovich, *Fluid Mechanics: A Short Course for Physicists* (Cambridge University Press, Cambridge, 2011).
- [34] R. Nedderman, in *Statics and Kinematics of Granular Materials* (Cambridge University Press, Cambridge, 1992), p. 352.
- [35] S. Fazekas, J. Török, and J. Kertész, *Phys. Rev. E* **75**, 011302 (2007).
- [36] N. Menon and D. J. Durian, *Science* **275**, 1920 (1997).
- [37] A. Daerr and S. Douady, *Nature (London)* **399**, 241 (1999).
- [38] F. Bonnet, T. Richard, and P. Philippe, *Granular Matter* **12**, 317 (2010).
- [39] J. Ren, J. A. Dijksman, and R. P. Behringer, *Phys. Rev. Lett.* **110**, 018302 (2013).
- [40] B. P. Tighe, *Granular Matter*, doi:10.1007/s10035-013-0436-6 (2013).
- [41] C. Li, T. Zhang, and D. I. Goldman, *Science* **339**, 1408 (2013).